

Characterization of Microstructure, Texture, and Microtexture in Near-Alpha Titanium Mill Products

A.L. PILCHAK, C.J. SZCZEPANSKI, J.A. SHAFFER, A.A. SALEM, and S.L. SEMIATIN

Microstructure, texture, and microtexture in Ti-6Al-2Sn-4Zr-2Mo-0.1Si billet/bar of three different diameters (57, 152, and 209 mm) were quantified using backscattered electron imaging and electron backscatter diffraction. All three billets exhibited a microstructure comprising a large fraction (≥ 70 pct) of primary alpha particles, the average size of which decreased and aspect ratio increased with increasing reduction/decreasing billet diameter, or trends suggestive of low final hot working temperatures and/or slow cooling rates after deformation. Appreciable radial variations in the volume fraction and aspect ratio of alpha particles were noticeable only for the smallest-diameter billet. Alpha-phase textures were typical of axisymmetric deformation, but were relatively weak ($\sim 3\times$ random) for all billet diameters. By contrast, bands of microtexture, which were multiple millimeters in length along the axial direction, were relatively strong for all of the materials. The intensity and radial thickness of the bands tended to decrease with decreasing billet diameter, thus indicating the important influence of imposed strain on the elimination of microtexture and the possible influence of surface preform microstructure following the beta quench on the evolution of microstructure and microtexture.

DOI: 10.1007/s11661-013-1804-x

© The Minerals, Metals & Materials Society and ASM International 2013

I. INTRODUCTION

TITANIUM and titanium alloys are used in a variety of aerospace, marine, and chemical industry applications.^[1] Many of these applications require the fabrication of components *via* operations such as closed-die forging, shape extrusion, conventional or high-speed machining (“hogout”), and superplastic forming. In turn, the microstructure, texture, and hence properties of the finished parts rely heavily on the uniformity and quality of mill products such as billet, plate, and sheet from which they are made.

Utilized for a substantial fraction of all aerospace applications, mill products of alpha/beta and near-alpha titanium alloys are usually synthesized *via* vacuum-arc or cold-hearth melting followed by casting in round (or rectangular) molds having cross-sectional dimensions of the order of 500 to 1000 mm.^[2] In the as-cast condition, the macrostructure consists typically of a thin, surface layer (“chill zone”) of fine, equiaxed beta grains surrounding regions of coarse columnar and equiaxed beta grains, the exact extent of each depending on the size of the ingot and casting conditions.^[3,4] The coarse,

columnar beta grains are typically multiple millimeters in diameter and length.

Following casting, the ingot structure is broken down by a series of thermomechanical (TMP) steps comprising hot working above the beta transus temperature (at which hcp alpha + bcc beta \rightarrow beta), initial alpha/beta working, beta recrystallization, and secondary alpha/beta working. The objective of the first three steps is to generate a uniform, recrystallized structure of equiaxed beta grains, the average size of which is ~ 1 mm. After the beta recrystallization treatment, titanium billets are usually water quenched, and the metastable high-temperature beta phase decomposes to form a transformation product that may vary from lamellar, colony alpha (at slow-to-moderate cooling rates at the interior) or acicular, possibly martensitic alpha (at rapid cooling rates experienced at and near the surface). Measurable non-uniformity in the microstructure and the texture of the alpha and beta phases may persist following these steps, however, because of heterogeneity in the initial macrostructure, unavoidable radial and axial strain variations associated with the upsetting and cogging operations used during hot working of ingots, and cooling-rate variations during the beta-quench operation.^[5]

Secondary alpha/beta hot working is imposed to spheroidize the colony/martensitic alpha, thereby producing a microstructure of fine equiaxed (“globular”) alpha particles in a matrix of single-phase beta or transformed beta. However, the effective strain levels required to complete spheroidization *during* deformation^[6] are typically much higher than those that can be imposed during secondary alpha/beta working (~ 1 to 1.5), except for preform microstructures which comprise fine acicular alpha.^[7–13] To a certain extent, the strain

A.L. PILCHAK and C.J. SZCZEPANSKI, Materials Research Engineers, and S.L. SEMIATIN, Senior Scientist, are with the Air Force Research Laboratory, Materials and Manufacturing Directorate, AFRL/RXCM, Wright Patterson Air Force Base, OH 45433-7817. Contact e-mail: adam.pilchak@wpafb.af.mil J.A. SHAFFER, Materials Research Engineer, and A.A. SALEM, CEO, are with the Materials Resources, LLC, Dayton, OH 45434.

Manuscript submitted December 4, 2012.

Article published online June 4, 2013

levels used in production are limited by the product size needed for subsequent part forging. Slow cooling following hot working or a post-hot working annealing treatment may bring about an increment of *static* spheroidization^[14] with the final alpha particle size being a strong function of the initial alpha-platelet thickness and the specific processing temperatures used during hot working and heat treatment.^[15] Nevertheless, it is not unusual to observe remnant, unspheroidized, “spaghetti” alpha with an aspect ratio (length:diameter) of 2:1 or greater in production-scale billets having diameters in the range of 150 to 300 mm. Furthermore, billet products may contain large regions characterized by many alpha particles with the same crystallographic orientation even if the microstructure appears to be fully (or partially) spheroidized. Known as microtextured regions (MTRs) or macrozones, these features were first documented in the 1990s concurrent with the development of high-speed automated techniques to measure local texture such as those based on electron backscatter diffraction (EBSD).^[16] Despite their obvious appearance in EBSD data, there have been relatively few attempts to quantitatively characterize the sizes and/or shapes of these regions.^[16–18]

Despite the fact that MTRs tend to have a deleterious effect on properties such as fatigue,^[19–22] only a relatively modest amount of effort has been expended to relate TMP parameters to the severity of the anomaly and to develop methods to obviate the problem. From a broad perspective, it appears that MTRs are primarily associated with specific prior-beta grains or colonies which have received relatively limited deformation. For example, it has been found that alpha colonies with a hard (*c*-axis) orientation relative to the applied stress tend to deform less (and hence spheroidize less) during hot working in comparison to softer colonies orientated such that prism or basal slip is activated.^[23] Additionally, colonies deforming by only basal or prism slip may also retain similar *c*-axis orientation and therefore be considered microtextured even if spheroidization occurs readily. The severity of MTR formation associated with the primary alpha (α_p) may be further exacerbated by the tendency of secondary (platelet) alpha to form on cooling such that its orientation is similar to that of the α_p particles.^[24–29] Methods to reduce the severity of MTRs include the use of very high strains during conventional high strain rate hot working to insure dynamic spheroidization, judicious changes in hot working direction and temperature to promote uniform straining of colonies of different orientations, and the introduction of superplastic flow to rotate and

randomize the orientation of α_p particles.^[23,30–33] It is noteworthy that the term “particle” is used as opposed to “grain” to emphasize that it is often not possible from conventional optical or electron imaging techniques to determine if a particle actually consists of multiple “grains” as defined by a particular misorientation angle from EBSD data.

To the present, there are few reports of the microtexture developed in commercially produced billet of alpha/beta and near-alpha alloys of various sizes, let alone the radial (or axial) variation in microtexture in such materials. Hence, the present work was undertaken to provide a quantitative measurement of typical variations in microstructure and microtexture for typical, production-scale Ti-6Al-2Sn-4Zr-2Mo-0.1Si billets and bars of various diameters.

II. MATERIALS AND EXPERIMENTAL PROCEDURES

Procured from various sources, the program materials comprised Ti-6Al-2Sn-4Zr-2Mo-0.1Si (Ti6242S) billet/bar product of three different diameters (57, 152, and 209 mm) with very similar measured compositions (Table I). The detailed processing histories of these materials were proprietary and largely unknown to the authors. Each material was electric discharge machined to obtain 10 mm × 10 mm longitudinal samples (containing the billet/bar axis and a radial direction) from the center, mid-radius, and outer diameter (OD). These samples were prepared metallographically using standard procedures starting with grinding on successively finer SiC papers to 1200 grit. Subsequently, each sample was electropolished in a solution of 350 mL butyl cellulose, 590 mL methanol, and 60 mL perchloric acid at a temperature of 223 K (−50 °C) and an applied potential of 22 V.

The microstructure of each sample was determined first using the backscattered electron (BSE) imaging mode in a scanning electron microscope (SEM) operated with an accelerating voltage of 20 kV and a probe current of ~10 nA. A minimum of five images was taken from each sample at the same axial position, but radial positions ~1 mm apart. These images were analyzed to obtain the volume fraction (V_f), size, and aspect ratio of primary α particles. For this purpose, V_f was obtained by overlaying a rectangular grid of points on each image and counting the number fraction which was inside a primary α particle. Line intercepts along axial, radial, and various random directions provided size statistics for the primary α particles.

Table I. Composition of the Ingot from Which the Program Materials Were Obtained

Billet (mm)	Al	Sn	Zr	Mo	Si	O	Fe	C	N	H
57	6.075	2.0	3.94	2.045	0.20	0.132	0.10	70	20	17
152	6.23	2.02	4.06	2.05	0.08	0.13	0.02	50	20	74
209	6.195	2.03	4.015	1.98	0.09	0.135	0.02	140	30	68

All elements are specified in weight pct, except C, N, and H which are reported in weight ppm.

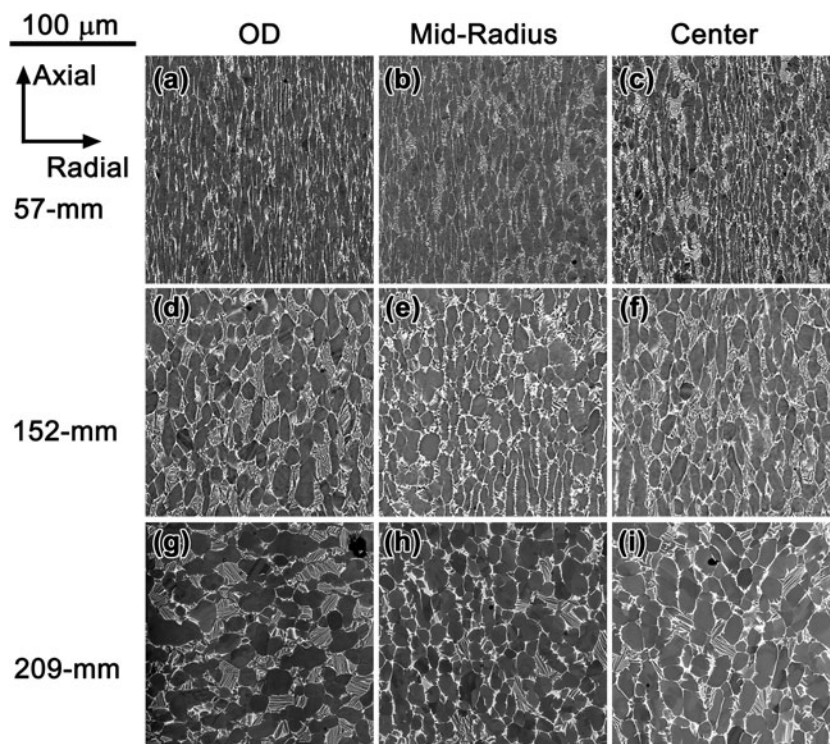


Fig. 1—Representative backscattered electron images of the microstructure in the bar and billet materials. Each row of images corresponds to a particular product diameter, while the each column of images corresponds to the position at which the image was taken.

The texture and microtexture of the billets/bar were quantified using large-area EBSD scans in an XL-30 SEM. Specifically, the analysis consisted of $\sim 2,000$ individual EBSD scans for each sample ($183 \mu\text{m} \times 183 \mu\text{m}$ each at $3\text{-}\mu\text{m}$ step size) using custom software to collect^[34] and combine^[35,36] the data. Once the data were combined into a single file, an orientation distribution function (ODF) describing the overall texture for each sample was calculated using standard spherical harmonics; pole figures were obtained from the ODFs to facilitate visualization of the textures. The degree of microtexture was assessed qualitatively from crystal-orientation maps (COMs) generated from the EBSD data. Subsequent quantitative analysis was conducted with the software TiZone™.^[37] This software identifies regions of microtexture using a two-step procedure. First, each pixel in a large EBSD scan is clustered into a group based on the spatial orientation of the c -axis. Next, a voting scheme is used to determine whether a particular point in each set of c -axis clusters is also spatially located near other pixels of similar c -axis orientation, thereby forming a microtexture region (MTR).

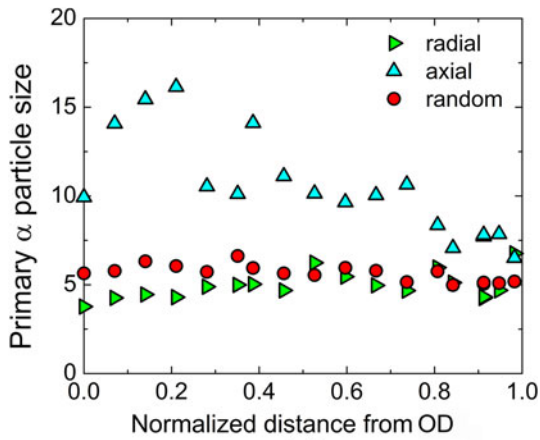
III. RESULTS AND DISCUSSION

The primary results of this research comprised spatially resolved measurements of the V_f , size, and aspect ratio of the primary α particles and the texture/microtexture of the α phase in each of the three Ti-6242S mill products used in this program.

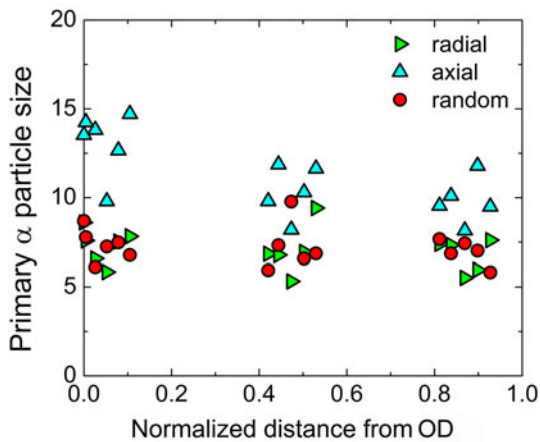
A. Microstructure

Representative BSE micrographs for the various radial locations (OD, mid-radius, and center) within the three lots of material (Figure 1) revealed the morphology of the primary α (α_p) particles and matrix phase. For the 57-mm-diameter bar (Figures 1(a) through (c)), the microstructure consisted of a large fraction of α_p particles which were noticeably elongated along the axial direction and a small fraction of matrix phase (of beta/transformed beta), the fineness of which increased with radial distance from the center. Slightly elongated α_p particles lying within a matrix of transformed beta (*i.e.*, prior-beta grains containing secondary alpha plates) were observed in the 152-mm-diameter billet (Figures 1(d) through (f)). In the 209-mm-diameter billet, the microstructures consisted of α_p particles which appeared nearly equiaxed (Figures 1(g) through (i)).

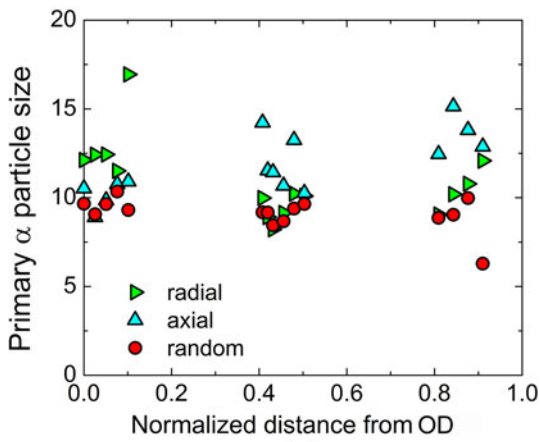
Despite significant scatter in individual measurements, semi-quantitative trends describing the location dependence of the microstructure were extracted from the BSE micrographs. In all of the plots, the radial coordinate on the abscissa was normalized by the outer radius of the billet/bar. Line-intercept measurements of the size of the α_p particles along axial, radial, and random directions are shown in Figure 2. Only the axial measurements of the α_p particle size appeared to vary systematically as a function of location within the billet for a given billet size. For the 57- and 152-mm-diameter samples, the average α_p particle size *decreased* moving from the OD to the center; the opposite trend, albeit



(a)



(b)



(c)

Fig. 2—Primary α particle size (in micrometers) as a function of normalized position and billet/bar diameter: (a) 57 mm, (b) 152 mm, and (c) 209 mm.

slight, was noted in the 209-mm billet. A more significant observation was that the radial α_p particle size measurements for each product size were essentially unchanged as a function of location. However, the small-diameter bar had an average radial particle size of $\sim 5 \mu\text{m}$, while this feature was slightly larger than $5 \mu\text{m}$ for the 152-mm billet and nearly $10 \mu\text{m}$ for the 209-mm billet. The α_p particle sizes measured with the randomly

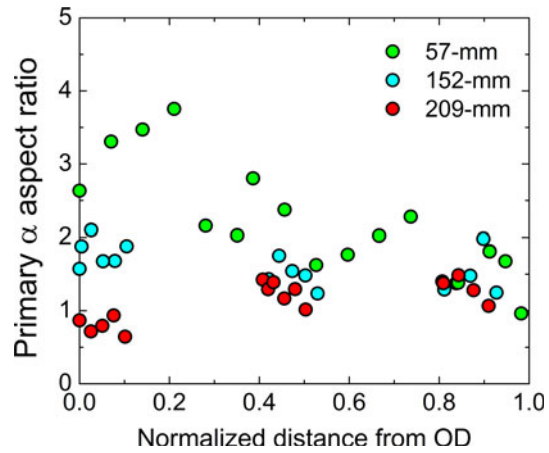


Fig. 3—Variation in primary α particle aspect ratio as a function of normalized position and billet/bar diameter.

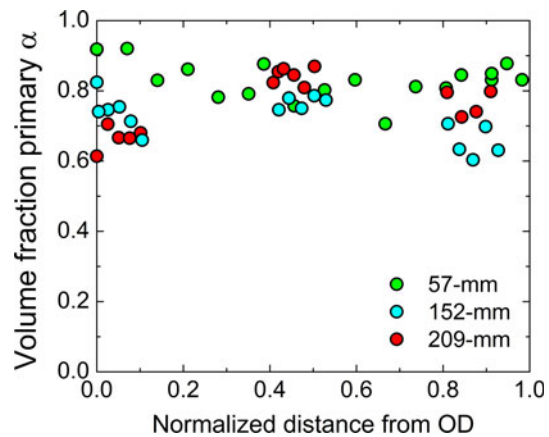


Fig. 4—Variation in primary α volume fraction as a function of normalized position and billet/bar diameter.

oriented lines replicated the measurements from the radial orientation, most likely because the particle size measurements in the radial orientation were much smaller than those in the axial direction.

The location dependence of microstructure was also visible in the aspect ratio measurements for each of the billet/bar products (Figure 3). The observed particle shape likely resulted from the specific forming operations used to produce each billet/bar; for example, both the 57- and 152-mm mill products were finished *via* radial forging, while the 209-mm billet was cogged. In addition, the higher α_p particle aspect ratios for the 57-mm-diameter bar may have been due to a higher degree of die chill during processing if secondary alpha/beta work had started at a small diameter.

The area fraction of α_p particles (Figure 4) appeared higher at the OD with a slight, but systematic, drop moving toward the center for both the 57-mm bar and the 152-mm billet. However, this trend was not observed for the 209-mm billet which may be related to the occurrence of deformation heating at specific locations during the conversion process.

B. Electron Backscatter Diffraction

1. Macrotecture

The nature and strength of the deformation texture developed during the thermomechanical processing of metallic materials such as titanium and titanium alloys are intimately related to their crystal symmetry/deformation mechanism and the applied strain and strain path. Various strain paths may be imposed during the production of titanium billet. However, each of these paths tends to reduce the diameter of the stock, resulting in an increase in length. Therefore, the overall strain path may be thought to be similar to extrusion which typically leads to a $10\bar{1}0$ alpha-phase partial fiber texture with the fiber axis parallel to the extrusion direction. Correspondingly, at all radial positions in an extrusion (or billet), there is an equal density of basal poles transverse to the fiber axis in a true $10\bar{1}0$ partial fiber texture as a consequence of crystallography and product symmetry. The symmetry associated with this fiber texture can be enforced by imposing axial sample symmetry artificially when determining the orientation distribution experimentally. Such “forcing” was not done in the present work, however. This enabled a clear picture of the detailed evolution of the $10\bar{1}0$ partial fiber at various stages in the fabrication of billets as a function of overall imposed reduction and radial strain non-uniformity within each mill product.

The degree of macrotecture of the alpha phase was relatively weak in all cases with maxima of $\sim 2\times$, $2.5\times$, and $3.5\times$ for the 152-, 209-, and 57-mm-diameter billets/bar, respectively (Figure 5). In particular, the macrotecture of the 209-mm-diameter billet was relatively nondescript with various low intensity peaks scattered throughout the (0001) pole figure. However, a small fraction of $(10\bar{1}0)$ poles was aligned with the billet axis in the OD and mid-radius locations. With increasing

strain (*i.e.*, for the smaller diameter billet and bar), the alignment of $(10\bar{1}0)$ poles with the billet axis became more evident at all locations; the partial fiber texture was strongest at the OD of the billet and weakest at the center.

The macrotecture observations were consistent with the local strain increasing from the center to the OD and the overall strain increasing with decreasing billet diameter. Further support for the increased strain is evident in the (0001) pole figures. With decreasing billet diameter and decreasing distance from the OD, the basal poles shifted from being widely distributed to being concentrated along the equator of the pole figure which corresponds to the radial directions in the billet/bar. In the center of the 57-mm bar, the transversely oriented basal poles were clustered, but this intensity was smoother and the distribution of basal poles around the fiber more uniform near the OD.

One unexpected texture component was also noted, namely, that described by $[0001]_z$ parallel to the billet axis. This component was most evident in the center of the 152-mm billet, but was also observed, although to a lesser extent, at the center and mid-radius positions in the 209-mm billet. This component can be formed by alpha particles with their *c*-axes parallel to the billet axis (“hard regions”) or by the preferential transformation from beta to alpha upon cooling from the processing temperature. A number of factors may influence variant selection during the allotropic transformation including local stresses developed by thermal expansion anisotropy^[25] and the presence of dislocations on highly active $\{110\}$ planes.^[38] Another work^[29] hypothesized that anisotropic contraction of primary alpha particles could cause slip on otherwise low resolved shear stress $\{110\}$ planes, *i.e.*, those perpendicular to the deformation axis, thus biasing these variants. Variant selection can also be

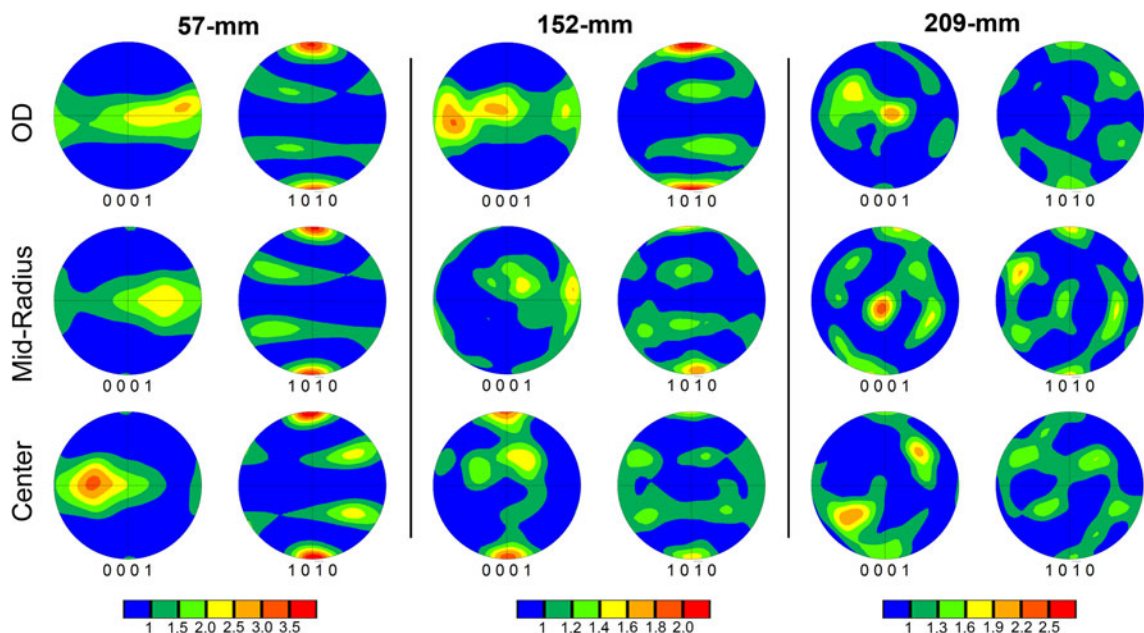


Fig. 5—Alpha phase (0001) and $(10\bar{1}0)$ pole figures showing the macrotecture as a function of position and billet/bar diameter. The sample reference frame is indicated by the axial (A) and radial (R) directions in the bar/billets.

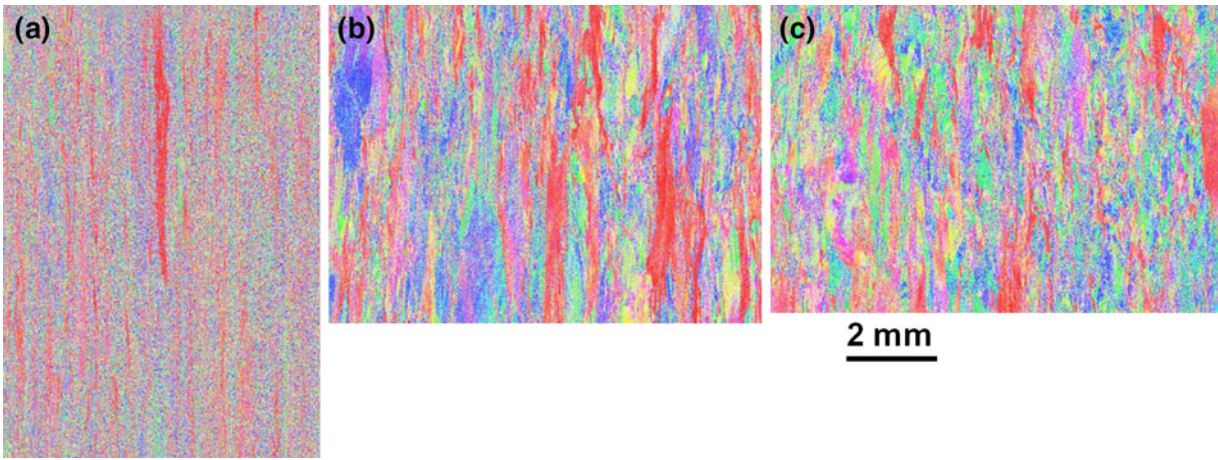


Fig. 6—Radial direction crystal-orientation maps for 209-mm-diameter billet: (a) OD, (b) mid-radius, and (c) center locations. The billet axis is vertical.

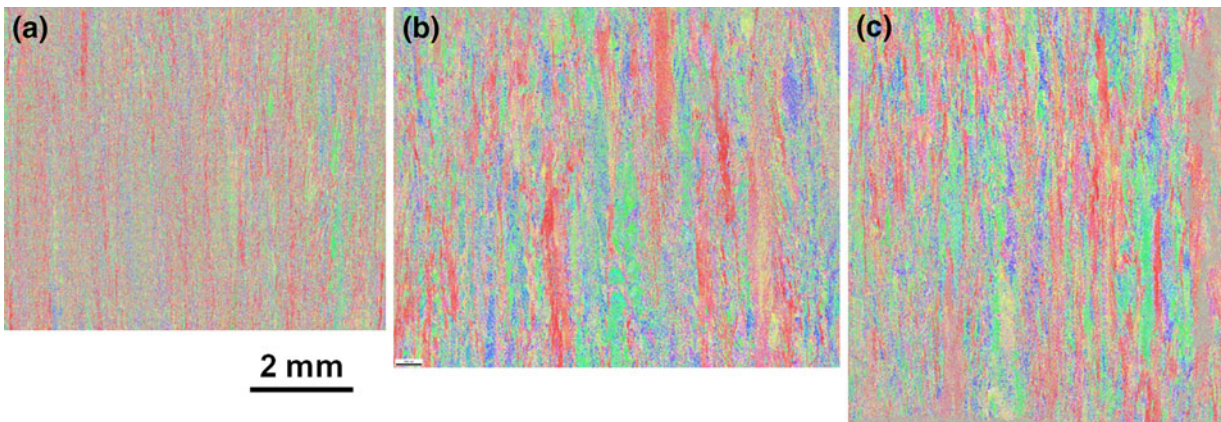


Fig. 7—Radial direction crystal-orientation maps for 152-mm-diameter billet: (a) OD, (b) mid-radius, and (c) center locations. The billet axis is vertical.

influenced by the presence of nearly parallel $\{110\}$ planes at β grain boundaries.^[39] These studies have indicated that many factors may influence variant selection, but to date there is no set of guidelines for the processing regimes where each one dominates. In the present work, the beta phase had a 110 partial fiber texture. As a result, there was a higher probability of having nearly parallel $\{110\}$ planes which may have mildly influenced the formation of the alpha-phase basal component parallel to the billet axis.

2. Microtexture

Radial direction COMs determined from the large-area EBSD scans (Figures 6, 7, 8) revealed the qualitative trends in MTR size within each billet as well as the changes in MTR between billets/bar of different diameters. Subtle changes in the size and shape of the MTRs were evident when comparing the center and mid-radius positions within each billet. Specifically, the MTRs appeared slightly more elongated and narrower at the mid-radius. In contrast to the observations for the center and mid-radius, however, large differences were found at the OD position. Here, the overall size of the

MTRs was reduced considerably, and much of the microstructure in the scanned area could be classified as randomly oriented. This is likely due to a combination of two factors. First, the near-surface position could have experienced higher strains during cogging/radial forging due to the choice of die design, reduction, bite, *etc.* Second, the near-surface region of the workpiece following a prior-beta-quench operation would have cooled more rapidly and thus formed finer α platelets/laths. This refined microstructure would have spheroidized more easily and ultimately became a finer MTR interspersed with a large fraction of random α_p particles generated by dynamic spheroidization.

More significant differences in the nature of MTRs were found when comparing the same normalized location in billets of different diameters. At all locations, it was found that the MTRs were significantly more highly elongated and narrower as the product diameter decreased for each radial location. This observation, in addition to the pole figure measurements, indicated that higher levels of strain do not necessarily eliminate microtexture once a stable texture component (in this case, the 10 $\bar{1}0$ partial fiber) is formed. Similar observations and

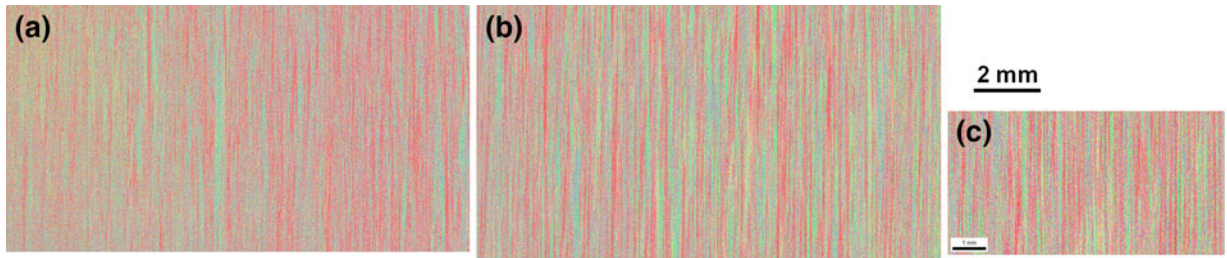


Fig. 8—Radial direction crystal-orientation maps for 57-mm-diameter bar: (a) OD, (b) mid-radius, and (c) center locations. The bar axis is vertical.

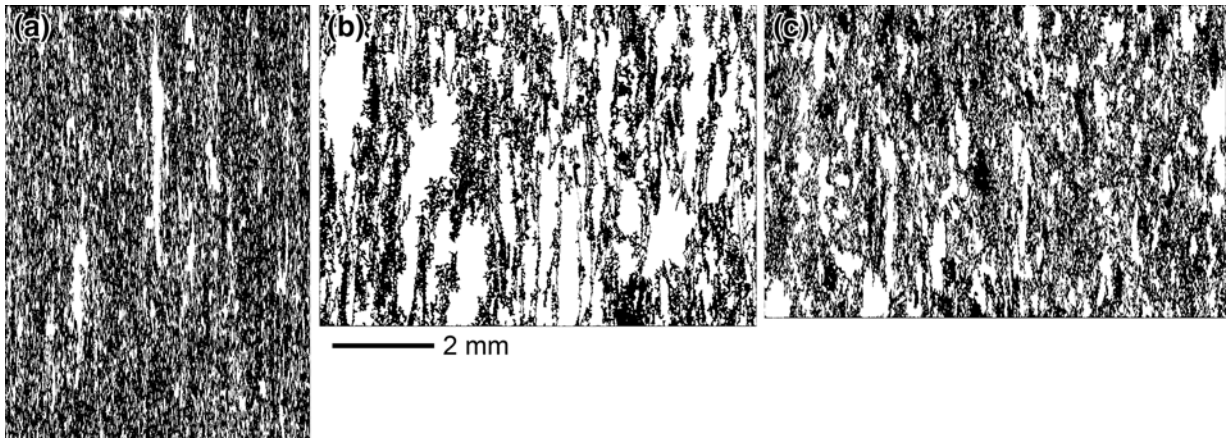


Fig. 9—Segmented MTRs (white) and outliers (black) for the 209-mm-diameter billet: (a) OD, (b) mid-radius, and (c) center locations. The billet axis is vertical.

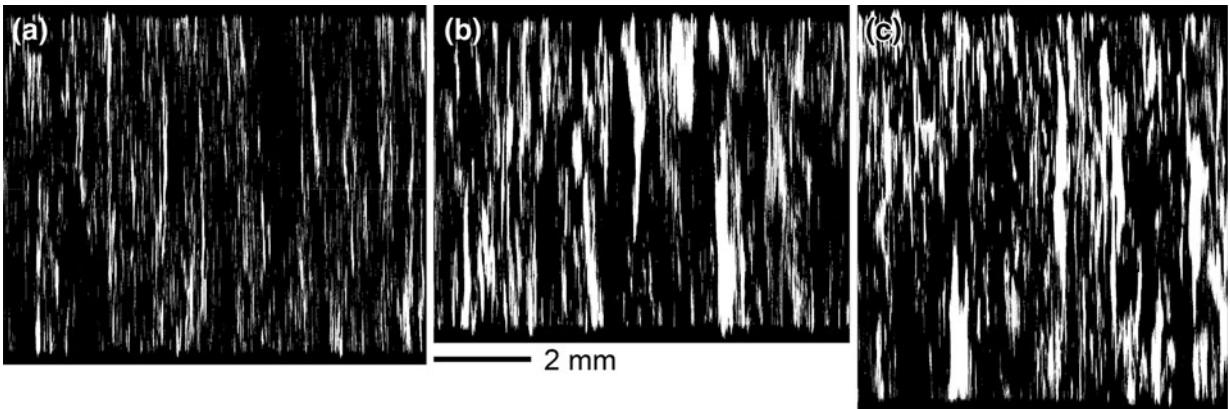


Fig. 10—Segmented MTRs (white) and outliers (black) for the 152-mm-diameter billet: (a) OD, (b) mid-radius, and (c) center locations. The billet axis is vertical.

actually an *increase* in the size of MTRs of stable texture components have been measured by Szczepanski *et al.*^[32]

The observed trends were quantified using the software TiZone™ to segment discrete MTRs in each of the nine datasets. The segmented MTRs in each sample (Figures 9, 10, 11) were then quantified using a two-point autocorrelation function.^[40] The autocorrelation function at position $(c + n, c + m)$, in which c denotes the center and n and m are horizontal and vertical

displacements, respectively, in real space, provides (in the frequency domain) the probability of a random vector projected in real space having its head and tail both lying within a MTR. The complete set of autocorrelations for the present samples formed a very large dataset, and thus the data were reduced using principal component analysis (PCA).^[41] PCA space represents a linear change of basis such that the highest data entropy (*i.e.*, a linear combination of the autocorrelation which has the greatest variance of the whole dataset) becomes

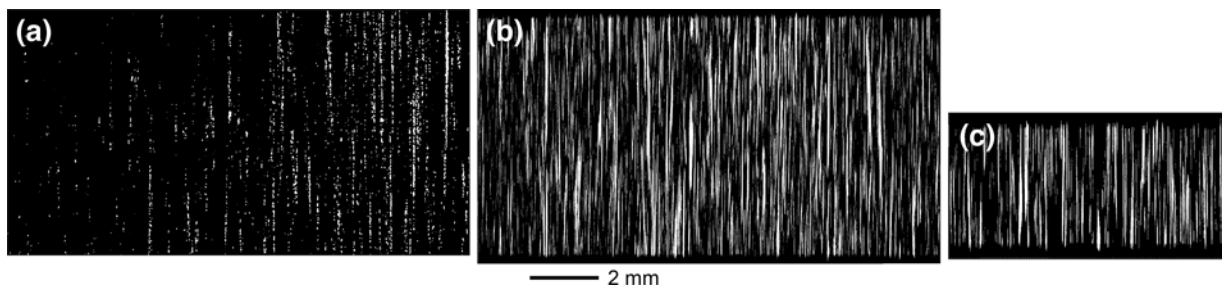


Fig. 11—Segmented MTRs (white) and outliers (black) for the 57-mm-diameter bar: (a) OD, (b) mid-radius, and (c) center locations. The bar axis is vertical.

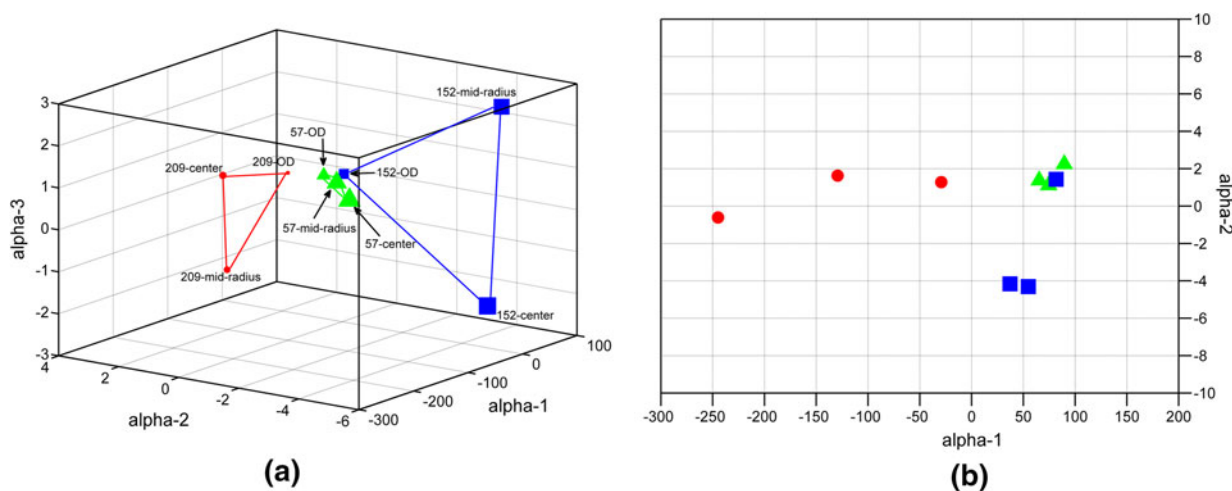


Fig. 12—(a) Visualization of the MTRs in PCA space. (b) Projection of PCA space exemplifying the heterogeneity in the 209-mm-diameter billet. Each point represents the entire dataset from each billet/bar. Points near one another represent similarity in structure.

Table II. One-Point Statistical Measures of MTR Thickness in Radial Direction

Sample	Mean (Std. Dev) (μm)	Median (μm)	Max (μm)	MTR (V_f)
57-OD	94 (38)	87	162	0.10
57-Mid-Radius	82 (17)	84	120	0.16
57-Center	77 (20)	75	115	0.13
152-OD	71 (20)	72	135	0.10
152-Mid-Radius	264 (83)	260	496	0.20
152-Center	239 (84)	216	393	0.24
209-OD	184 (65)	174	537	0.36
209-Mid-Radius	821 (196)	840	1314	0.61
209-Center	377 (112)	351	672	0.49

the first vector in the new vector basis and the second vector has the next highest data entropy while simultaneously being orthogonal to the first, *etc.* This process is repeated for rank, preserving orthogonality. The first three dimensions of the principal components are shown in Figure 12. Inspection of the PCA space revealed that the scans taken near the OD of each of the three different product forms had the smallest symbols and were all clustered together, thus indicating the similar character of the MTRs at this location. This finding also indicated that the MTRs in all OD scans were very similar, implying that the MTRs near the surface were not reduced in size by imposing more strain. On the

other hand, the MTRs at the mid-radius and center locations in the 152- and 209-mm-diameter billets were widely distributed in PCA space, thus highlighting the difference in the character of microtexture at these locations. The initial separation of the three sample positions for the larger diameter billets and the clustering of all three locations in the smallest-diameter billet suggested that the MTRs in the interior of the billets were most affected by strain level. The plane in PCA space containing all three data points is known as a hull. The size of the hull for each billet served as a measure of the overall heterogeneity within that billet. While not apparent in Figure 12(a), the large variations in the first

principal component between scan locations in the 209-mm billet are clearly visible in the projection of PCA space shown in Figure 12(b). These data reveal a clear trend whereby heterogeneity decreases with billet diameter.

While PCA space is useful in visualizing differences in the datasets, the physical dimensions of the regions are needed to be used in processing or life-prediction models. Thus, the volume fraction and several measures of MTR thickness were extracted from the segmented MTR images using line intercepts in the radial (horizontal) direction. As shown in Table II, there is a general trend in the mean, median, and maximum measurements where the MTRs become smaller for a particular location with decreasing billet diameter. There are a few exceptions, however, to this trend. For instance, the OD location in the 57-mm billet is larger than in the 152-mm billet. The mean and median measurements in the mid-radius position of the 152- and 209-mm billets were larger than in the center. Indeed, the COMs (Figures 6(a) and 7(a)) from these locations suggest that there are larger, more intense regions of similar orientation. This trend is also reflected in segmented MTR images (Figures 9(a) and 10(a)) where large regions were clustered as opposed to many smaller clusters.

IV. SUMMARY AND CONCLUSIONS

The variation in (1) microstructure, (2) texture, and (3) microtexture of Ti-6242 forging stock with diameters of 57, 152, and 209 mm was investigated by means of SEM and EBSD. The following observations were made:

- (1) The average primary α particle size decreased by ~25 pct from ~10 μm in the 209-mm billet to ~7.5 μm in 152-mm billet and was further refined to ~5 μm in the 57-mm bar. The primary alpha aspect ratio increased as the bar/billet diameter was reduced and also increased with decreasing distance from the OD. One notable exception was the surface of the 209-mm billet. There were no clear trends in the volume fraction of primary alpha in the larger diameter billets, but the radial variations in the experimental observations may be qualitatively explained by deformation heating and/or chilling during processing. Deformation heating near the surface of large diameter billets processed by radial forging tends to lead to lower alpha volume fractions compared to the center which may cool from the preheat temperature. In contrast, surface chilling is more significant in the 57-mm bar leading to higher volume fractions of primary alpha which accommodate more of the deformation, resulting in elongated alpha particles.
- (2) The macrotexture measured in each location was generally weak, *i.e.*, less than $3\times$ random when averaged over large areas. When considered in the order of increasing continuum level strain, the texture approached the (10 $\bar{1}$ 0) partial fiber texture expected for axisymmetric extrusion of HCP metals.

- (3) Despite an overall weak macrotexture, high aspect ratio microtexture regions (MTRs) were present at all locations in all of the billets/bar. The regions were segmented from EBSD data after which their thickness was quantified with radial direction line intercepts. The size, shape, and spatial distribution of the MTRs at each position in the billets/bar were quantified and compared using principal component analysis. Clustering of the OD locations for all product forms in PCA space showed that the size and morphology of the near-surface MTRs were not significantly altered despite differences in composition, primary alpha characteristics, and processing path.

ACKNOWLEDGMENTS

This work was performed as part of the in-house research activities of the Air Force Research Laboratory's Materials and Manufacturing Directorate. The support and encouragement of the Laboratory management are gratefully acknowledged. One of the authors (ALP) also wishes to acknowledge support from the Air Force Office of Scientific Research (Task#12RX01COR, Dr. Ali Sayir, program manager). The assistance of J.C. Mossing, A. Blankenship, and M. Ahrens with sample preparation and image analysis is appreciated. Two of the authors (JAS and AAS) were supported through Air Force Contract FA8650-07-D-5800.

REFERENCES

1. G. Lütjering and J.C. Williams: *Titanium*, Springer Verlag, Berlin, 2007.
2. S.L. Semiatin, V. Seetharaman, and I. Weiss: in *Advances in the Science and Technology of Titanium Alloy Processing*, I. Weiss, R. Srinivasan, P.J. Bania, D. Eylon, and S.L. Semiatin, eds., TMS, Warrendale, PA, 1997, pp. 3–73.
3. M.G. Glavicic, P.A. Kobryn, F. Spadafora, and S.L. Semiatin: *Mater. Sci. Eng. A*, 2003, vol. A346, pp. 8–18.
4. A.N. Kalinyuk, N.P. Trigub, V.N. Zamkov, O.M. Ivasishin, P.E. Markovsky, R.V. Teliovich, and S.L. Semiatin: *Mater. Sci. Eng. A*, 2003, vol. A346, pp. 178–88.
5. M.G. Glavicic, P.A. Kobryn, R.L. Goetz, K.O. Yu, and S.L. Semiatin: in *Ti-2003: Science and Technology*, G. Luetjering and J. Albrecht, eds., Wiley-VCH Verlag GmbH, Weinheim, 2004, pp. 1299–307.
6. S.L. Semiatin, V. Seetharaman, and I. Weiss: *Mater. Sci. Eng. A*, 1999, vol. A263, pp. 257–71.
7. E.B. Shell and S.L. Semiatin: *Metall. Mater. Trans. A*, 1999, vol. 30A, pp. 3219–29.
8. H. Inagaki: *Z. für Metallkunde*, 1995, vol. 86, pp. 643–50.
9. C.H. Park, K.-T. Park, D.H. Shin, and C.S. Lee: *Mater. Trans.*, 2008, vol. 49 (10), pp. 2196–2200.
10. K. Wang, W. Zeng, Y. Zhao, Y. Shao, and Y. Zhou: *Mater. Sci. Eng. A*, 2010, vol. A527, pp. 6193–99.
11. K. Wang, W. Zeng, Y. Zhao, Y. Lai, and Y. Zhou: *Mater. Sci. Eng. A*, 2010, vol. A527, pp. 2259–566.
12. H.-W. Song, S.-H. Zhang, and M. Cheng: *J. Alloys Compd.*, 2009, vol. 480, pp. 922–27.
13. X. Ma, W. Zeng, F. Tian, and Y. Zhou: *Mater. Sci. Eng. A*, 2012, vol. A548, pp. 6–11.
14. N. Stefansson, S.L. Semiatin, and D. Eylon: *Metall. Mater. Trans. A*, 2002, vol. 33A, pp. 3527–34.

15. S.L. Semiatin, N. Stefansson, and R.D. Doherty: *Metall. Mater. Trans. A*, 2005, vol. 36A, pp. 1372–76.
16. A.P. Woodfield, M.D. Gorman, R.R. Corderman, J.A. Sutliff, and B. Yamrom: in *Titanium'95: Science and Technology*, P.A. Blenkinsop, W.J. Evans, and H.M. Flower, eds., Institute of Materials, London, 1995, pp. 1116–23.
17. L. Toubal, P. Bocher, A. Moreau, and D. Levesque: *Metall. Mater. Trans. A*, 2010, vol. 41A, pp. 744–50.
18. A. Bhattacharjee, A.L. Pilchak, O.I. Lobkis, J.W. Foltz, S.I. Rokhlin, and J.C. Williams: *Metall. Mater. Trans. A*, 2011, vol. 42A, pp. 2358–72.
19. A.L. Pilchak and J.C. Williams: *Metall. Mater. Trans. A*, 2011, vol. 42A, pp. 1000–27.
20. C.J. Szczepanski, S.K. Jha, J.M. Larsen, and J.W. Jones: *Metall. Mater. Trans. A*, 2008, vol. 39A, pp. 2841–51.
21. V. Sinha, J.E. Spowart, M.J. Mills, and J.C. Williams: *Metall. Mater. Trans. A*, 2006, vol. 37A, pp. 1507–18.
22. K. LeBiavant, S. Pommier, and C. Prioul: *Fatigue Fract. Eng. Mater. Struct.*, 2002, vol. 25, pp. 527–45.
23. T.R. Bieler and S.L. Semiatin: *Int. J. Plast.*, 2002, vol. 18, pp. 1165–89.
24. H. Moustahfid, N. Gey, M. Humbert, and M.J. Philippe: *Metall. Mater. Trans. A*, 1997, vol. 28A, pp. 51–59.
25. S.V. Divinski, V.N. Dnieprenko, and O.M. Ivasishin: *Mater. Sci. Eng. A*, 1998, vol. A243, pp. 201–05.
26. L. Germain, N. Gey, M. Humbert, P. Bocher, and M. Jahazi: *Acta Mater.*, 2005, vol. 53, pp. 3535–43.
27. M. Humbert, L. Germaine, N. Gey, P. Bocher, and M. Jahazi: *Mater. Sci. Eng. A*, 2006, vol. A430, pp. 157–64.
28. L. Germain, N. Gey, M. Humbert, P. Vo, M. Jahazi, and P. Bocher: *Acta Mater.*, 2008, vol. 56, pp. 4298–4308.
29. L. Zeng and T.R. Bieler: *Mater. Sci. Eng. A*, 2005, vol. A392, pp. 403–14.
30. G. Lutjering: *Mater. Sci. Eng. A*, 1998, vol. A243 (1998), pp. 32–45.
31. N. Gey, P. Bocher, E. Uta, L. Germain, and M. Humbert: *Acta Mater.*, 2012, vol. 60, pp. 2647–55.
32. C.J. Szczepanski, J.M. Larsen, and S.L. Semiatin: unpublished research, 2010.
33. G.A. Salishchev, O.R. Valiakhmetov, and R.M. Galeyev: *J. Mater. Sci.*, 1993, vol. 28, pp. 2898–902.
34. A.R. Shiveley, P.A. Shade, A.L. Pilchak, J.S. Tiley, and R. Kerns: *J. Microsc.*, 2011, vol. 244 (2), pp. 181–86.
35. A.L. Pilchak, A.R. Shiveley, J.S. Tiley, and D.L. Ballard: *J. Microsc.*, 2011, vol. 244 (1), pp. 38–44.
36. A.L. Pilchak, A.R. Shiveley, P.A. Shade, J.S. Tiley, and D.L. Ballard: *J. Microsc.*, 2012, vol. 248 (2), pp. 172–86.
37. A.A. Salem and J.A. Shaffer: TiZone™, Patent Pending, Materials Resources LLC, Dayton, OH, 2012.
38. N. Gey, M. Humbert, M.J. Philippe, and Y. Combres: *Mater. Sci. Eng. A*, 1997, vol. A230, pp. 68–74.
39. D. Bhattacharyya, G.B. Viswanathan, R. Denkenberger D. Furrer, and H.L. Fraser: *Acta Mater.*, 2003, vol. 51, pp. 4679–91.
40. S. Torquato: *Random Heterogeneous Materials*, Springer-Verlag, New York, 2002.
41. S.R. Kalidindi, S.R. Niezgodna, and A.A. Salem: *JOM*, 2011, vol. 63 (4), pp. 34–41.